

# Interpreting the High Frequency QPO Power Spectra of Accreting Black Holes

Jeremy D. Schnittman

*Department of Physics, Massachusetts Institute of Technology*

*77 Massachusetts Avenue, Cambridge, MA 02139*

schnittm@mit.edu

## ABSTRACT

In the context of a relativistic hot spot model, we investigate different physical mechanisms to explain the behavior of quasi-periodic oscillations (QPOs) from accreting black holes. The locations and amplitudes of the QPO peaks are determined by the ray-tracing calculations presented in Schnittman & Bertschinger (2004a): the black hole mass and angular momentum give the geodesic coordinate frequencies, while the disk inclination and the hot spot size, shape, and overbrightness give the amplitudes of the different peaks. In this paper additional features are added to the existing model to explain the broadening of the QPO peaks as well as the damping of higher frequency harmonics in the power spectrum. We present a number of analytic results that closely agree with more detailed numerical calculations. Four primary pieces are developed: the addition of multiple hot spots with random phases, a finite width in the distribution of geodesic orbits, Poisson sampling of the detected photons, and the scattering of photons from the hot spot through a corona of hot electrons around the black hole. Finally, the complete model is used to fit the observed power spectra of both type A and type B QPOs seen in XTE J1550-564, giving confidence limits on each of the model parameters.

*Subject headings:* black hole physics – accretion disks – X-rays:binaries

## 1. INTRODUCTION

One of the most exciting results from the Rossi X-Ray Timing Explorer (RXTE) was the discovery of high frequency quasi-periodic oscillations (HFQPOs) from neutron star and black hole binaries (Strohmayer et al. 1996; Strohmayer 2001; Lamb 2002). For black hole

systems, these HFQPOs are observed repeatedly at more or less constant frequencies, and in a few cases with integer ratios (Remillard et al. 2002; Homan et al. 2004; Remillard et al. 2004). These discoveries give the exciting prospect of determining a black hole’s mass and spin, as well as testing general relativity in the strong-field regime.

To understand these observations more quantitatively, we have developed a ray-tracing code to model the X-ray light curve from a collection of “hot spots,” small regions of excess emission moving on geodesic orbits (Schnittman & Bertschinger 2004a,b). This hot spot model is motivated by the similarity between the QPO frequencies and the black hole coordinate frequencies near the inner-most stable circular orbit (ISCO) (Stella & Vietri 1998, 1999), as well as the suggestion of a resonance leading to integer commensurabilities between these coordinate frequencies (Abramowicz & Kluzniak 2001, 2003). Stella & Vietri (1999) investigated primarily the QPO frequency pairs found in LMXBs with a neutron star accretor, but their approach can be applied to black hole systems as well.

The basic geodesic hot spot model is characterized by the black hole mass and spin, the disk inclination angle, and the hot spot size, shape, and overbrightness. Motivated by the 3:2 frequency commensurabilities observed in QPOs from XTE J1550-564, GRO J1655-40, and H1743-322 (Remillard et al. 2002; Homan et al. 2004; Remillard et al. 2004), we pick a radius for the geodesic orbits such that the coordinate frequencies  $\nu_\phi$  and  $\nu_r$  will have a 3:1 ratio. Thus the 3:2 commensurability is interpreted as the fundamental orbital frequency  $\nu_\phi$  and its beat mode with the radial frequency at  $\nu_\phi - \nu_r$ . Together with the assumption that the concurrent low frequency QPOs are due to Lense-Thirring precession at this same radius (Stella et al. 1999), the location of the QPO peaks uniquely determines the black hole mass and spin. Relaxing the low frequency QPO criterion leaves a one-dimensional degeneracy in the mass-spin parameter space which can be broken by an independent determination of the binary system’s inclination and radial velocity measurements of the low-mass companion star [e. g., Orosz et al. (2002, 2004)].

Given the black hole mass, spin, inclination, and the radius of the geodesic orbit, the parameters of the hot spot model (i. e. the hot spot size, shape, and overbrightness, and the orbital eccentricity) are determined by fitting to the amplitudes of the peaks in the observed power spectrum. However, the model as described so far produces a perfectly periodic X-ray light curve as the single hot spot orbits the black hole indefinitely. Such a periodic light curve will give a power spectrum composed solely of delta-function peaks (Schnittman & Bertschinger 2004a), unlike the broad features in the observations.

In this paper we introduce two simple physical models to account for this broadening of the QPO peaks. The models are based on analytic results, then tested and confirmed by comparison with the three-dimensional ray-tracing calculations of multiple hot spots

(Schnittman & Bertschinger 2004b). These results draw repeatedly from the convolution theorem of complex Fourier analysis, an essential tool for relating the behavior of the physical system in the time domain with the more easily measured power spectrum in the frequency domain. We find the power spectrum can be accurately modeled by a superposition of Lorentzian peaks, consistent with the standard analysis of QPO data from neutron stars and black holes (Nowak 2000; Belloni et al. 2002). Many of the methods and results presented here are equally valid for other QPO models such as diskoseismology (Wagoner, Silbergleit, & Ortega-Rodriguez 2001), vertically-integrated disk oscillations (Rezzolla et al. 2003), toroidal perturbations (Lee & Ramirez-Ruiz 2002; Lee et al. 2004), and magnetic resonances (Wang et al. 2003).

In Section 2, we derive the effect of summing the light curves from multiple hot spots with random phases and different lifetimes to give a Lorentz-broadened peak in the power spectrum. Section 3 shows how a finite width in the radii of the geodesic orbits produces a corresponding broadening of the QPO peaks. In Section 4 we develop two simple models for detector statistics and photon scattering, both of which affect other features of the power spectrum such as the continuum noise and the damping of high frequency harmonics, but do not contribute to the broadening of the QPO peaks. Finally, all the pieces of the model are brought together in Section 5 and used to interpret the power spectra from a number of observations of XTE J1550-564. We conclude with a discussion of open questions for the hot spot model as well as directions for future work.

## 2. PEAK BROADENING FROM RANDOM PHASES

In this section we derive the shape of a QPO peak in Fourier space broadened by the summation of multiple periodic functions combined with random phases. There are many different accepted conventions for discrete and continuous Fourier transforms (Press et al. 1997), so we begin by defining the forward- and reverse-transforms between the time and frequency domains ( $t$  and  $\nu$ ). For a Fourier pair  $f(t)$  and  $F(\nu)$ ,

$$F_j = \frac{1}{N_s} \sum_{k=0}^{N_s-1} f_k e^{-2\pi i j k / N_s} \rightarrow F(\nu) = \frac{1}{T_f} \int_0^{T_f} f(t) e^{-2\pi i \nu t} dt \quad (1)$$

and

$$f_k = \sum_{j=0}^{N_s-1} F_j e^{2\pi i j k / N_s} \rightarrow f(t) = T_f \int_{-\nu_N}^{\nu_N} F(\nu) e^{2\pi i \nu t} d\nu, \quad (2)$$

where  $f(t)$  is defined on the time interval  $[0, T_f]$  and  $\nu_N = 1/(2\Delta t)$  is the Nyquist frequency for a sampling rate  $\Delta t = T_f/N_s$ . With this convention,  $f(t)$  and  $F(\nu)$  conveniently have the

same units and Parseval's theorem takes the form

$$\int_0^{T_f} f^2(t)dt = T_f^2 \int_{-\nu_N}^{\nu_N} F^2(\nu)d\nu. \quad (3)$$

For such a time series  $f(t)$ , the power spectrum is defined as  $F^2(\nu)$ , the squared amplitude of the Fourier transform.

Consider a purely sinusoidal function

$$f(t) = A \sin(2\pi\nu_0 t + \phi), \quad (4)$$

where  $\phi$  is some constant phase. If there are an integer number of complete oscillations within the time  $T_f$  or in the limit of  $T_f \rightarrow \infty$ , the Fourier transform of  $f(t)$  will be

$$F(\nu) = \begin{cases} \frac{A}{2}e^{i(\phi-\pi/2)} & \nu = \nu_0 \\ \frac{A}{2}e^{-i(\phi-\pi/2)} & \nu = -\nu_0 \\ 0 & \text{otherwise} \end{cases}. \quad (5)$$

If we then truncate the function  $f(t)$  by multiplying it with a boxcar window function  $w(t)$  of length  $\Delta T$ , the convolution theorem gives the transform of the resulting function  $g(t)$ :

$$g(t) = f(t)w(t) \Leftrightarrow G(\nu) = (F \star W)(\nu). \quad (6)$$

In the case where the window function is longer than a single period and short compared to the total sampling time ( $1/\nu_0 < \Delta T \ll T_f$ ), the convolved power  $G^2(\nu)$  can be approximated by

$$G^2(\nu) \approx \frac{A^2}{4T_f^2} \frac{\sin^2[\pi(\nu \pm \nu_0)\Delta T]}{\pi^2(\nu \pm \nu_0)^2}. \quad (7)$$

For  $f(t)$  real,  $F(-\nu) = F^*(\nu)$  and since we are primarily concerned with the power spectrum  $F^2(-\nu) = F^2(\nu)$ , we will consider only positive frequencies in the analysis below (unless explicitly stated otherwise). Of course, when calculating the actual observable power in a signal, both positive and negative frequencies must be included.

All the information about the phase  $\phi$  of  $f(t)$  and the location in time of the window function is contained in the complex phase of the function  $G(\nu)$ . This phase information is important when considering the total power contributed by a collection of signals, each with a different time window and random phase. When summing a series of complex functions with random phase, the total amplitude adds in quadrature as in a two-dimensional random walk. Therefore combining  $N$  different segments of  $f(t)$ , each of length  $\Delta T$  and random  $\phi$ , gives a Fourier transform with amplitude  $\sqrt{N}|G(\nu)|$ , and thus the net power spectrum is  $NG^2(\nu)$ .

The result in equation (7) is valid only if every segment of  $f(t)$  has the exact same sampling length  $\Delta T$  and frequency  $\nu_0$ . This is not necessarily the case in the context of the hot spot model, in which small regions of excess emission move along geodesic orbits, modulating the flux periodically as photons are relativistically beamed toward the observer. Three-dimensional MHD simulations of accretion disks suggest that in general such hot spots are continually being formed and destroyed with random phases, with a range of lifetimes and orbital frequencies (Hawley & Krolik 2001; De Villiers, Hawley, & Krolik 2003).

For now, we consider the contribution from identical hot spots, assuming that each one forms around the same radius with similar size and overbrightness and survives for some finite time before being destroyed. Over this lifetime, the hot spot produces a coherent periodic light curve sampled by a window function of duration  $T$ . Analogous to radioactive decay processes, we assume that during each time step  $dt$ , the probability of the hot spot dissolving is  $dt/T_l$ , where  $T_l$  is the characteristic lifetime of the hot spots. In this case, the differential probability distribution of lifetimes  $T$  for coherent segments is

$$P(T)dT = \frac{dT}{T_l} e^{-T/T_l}. \quad (8)$$

Over a sample time  $T_f \gg T_l$ , if there are an average of  $N_{\text{spot}}$  hot spots in existence at any time, the number of hot spots formed with a lifetime between  $T$  and  $T + dT$  is given by

$$dN(T) = N_{\text{spot}} \frac{T_f}{T_l^2} e^{-T/T_l} dT. \quad (9)$$

Assuming for the time being that each coherent section of the light curve is given by the sinusoidal  $f(t)$  used above, we can sum all the individual segments to give the total light curve  $I(t)$  with corresponding power spectrum

$$\begin{aligned} \tilde{I}^2(\nu) &= \int_0^\infty G^2(\nu, T) dN(T) \\ &= N_{\text{spot}} \left( \frac{A}{2\pi T_f} \right)^2 \int_0^\infty \frac{\sin^2[\pi(\nu - \nu_0)T]}{\pi^2(\nu - \nu_0)^2} \frac{T_f}{T_l^2} e^{-T/T_l} dT \\ &= 2N_{\text{spot}} A^2 \frac{T_l}{T_f} \frac{1}{1 + 4\pi^2 T_l^2 (\nu - \nu_0)^2}. \end{aligned} \quad (10)$$

Hence we find the shape of the resulting spectrum is a Lorentzian peaked around  $\nu_0$  with characteristic width

$$\Delta\nu = \frac{1}{2\pi T_l}. \quad (11)$$

If this model is a qualitatively accurate description of how hot spots form and dissolve in the disk, one immediate conclusion is that the oscillator quality factor  $Q$  can be fairly

high even for relatively short coherence times:

$$Q \equiv \frac{\nu_0}{\text{FWHM}} = \pi T_l \nu_0. \quad (12)$$

For example, if every hot spot has a lifetime of exactly four orbits ( $T_l = 4/\nu_0$ ), the central peak of the power spectrum  $G^2(\nu, T_l)$  has coherence  $Q = 4.5$ , about what one would expect from a first-order estimate. However, after integrating over the exponential lifetime distribution to get the Lorentzian profile of equation (10), the resulting quality factor is  $Q = 12.6$ , roughly a factor of three higher. Remillard et al. (2002) observe quality values of  $Q \sim 5 - 10$  for the HFQPOs seen in XTE J1550-564, corresponding to typical hot spot lifetimes of only 2-3 orbits.

In addition to the boxcar window, we have also tried other sampling functions to model the lifetime and evolution of the hot spots. Since the boxcar window represents an instantaneous formation and subsequent destruction mechanism, the resulting power spectrum contains significant power at high frequencies, a general property of discontinuous functions.

A smoother, Gaussian window function in time gives a Gaussian profile in frequency space:

$$w(t) = \exp\left(\frac{-t^2}{2T^2}\right) \Leftrightarrow W(\nu) = \sqrt{2\pi} \frac{T}{T_f} \exp\left(\frac{-\nu^2}{2\Delta\nu^2}\right) \quad (13)$$

where again the characteristic width is given by  $\Delta\nu = 1/(2\pi T)$ . After integrating over the same distribution of lifetimes  $dN(T)$  as above, we get the power spectrum

$$\tilde{I}^2(\nu) = 4\pi N_{\text{spot}} A^2 \frac{T_l}{T_f} z^3 \left[ \sqrt{\pi}(1 + 2z^2) \text{erfc}(z) e^{z^2} - 2z \right], \quad (14)$$

where we have defined

$$z \equiv \frac{1}{4\pi T_l (\nu - \nu_0)}. \quad (15)$$

For large  $z$  (near the peak at  $\nu = \nu_0$ ), equation (14) can be approximated by the narrow Lorentzian

$$\tilde{I}^2(\nu) \approx 4\pi N_{\text{spot}} A^2 \frac{T_l}{T_f} \frac{1}{1 + 48\pi^2 T_l^2 (\nu - \nu_0)^2}. \quad (16)$$

As with the boxcar window, the exponential lifetime distribution has the effect of narrowing the peak of the net power spectrum compared with that of a single segment of the light curve with length  $T_l$ . This smaller width can be understood by considering the distribution of hot spot lifetimes [eqn. (9)] and their relative contribution to the total power spectrum [eqns. (7, 13)]. While there are actually more segments with individual lifetimes shorter than  $T_l$ , the few long-lived segments of the light curves add significantly more weight to the QPO peaks since  $W(\nu = 0, T) \propto T$  while  $\Delta\nu \propto 1/T$ .

In fact, for any set of self-similar sampling functions  $w(t, T) = w(t/T)$ , the corresponding power spectra  $W^2(\nu, T)$  can be approximated near  $\nu = 0$  as a Lorentzian:

$$W^2(\nu, T) \approx \frac{T^2}{T_f^2} \frac{1}{1 + \beta^2 T^2 \nu^2}, \quad (17)$$

with  $\beta$  a dimensionless constant over the set of  $w(t, T)$ . The characteristic width of  $W^2(\nu, T)$  is thus defined as  $1/(\beta T)$ . Integrating over the lifetime distribution  $dN(T)$ , the net power function is given by

$$\tilde{I}^2(\nu) \approx \tilde{I}^2(\nu_0) \frac{1}{1 + 12\beta^2 T_l^2 (\nu - \nu_0)^2}. \quad (18)$$

We see now that the general effect of an exponential distribution of sampling lifetimes is to decrease the peak width, and thus increase the coherency, by a factor of  $\sqrt{12} \approx 3.5$ .

In addition to the boxcar and Gaussian windows, another physically reasonable model for the hot spot evolution is that of a sharp rise followed by an exponential decay, perhaps caused by magnetic reconnection in the disk. In this case, the light curve would behave like a damped harmonic oscillator, for which the power spectrum is also given by a Lorentzian. Interestingly, the resulting QPO peak width is exactly the same, whether we use a collection of boxcar functions with an exponential lifetime distribution, or if we use a set of exponential sampling functions, each with the same decay time. In the discussion below, we will assume a boxcar sampling function and an exponential lifetime distribution, with its corresponding Lorentzian power spectrum. This also facilitates a direct comparison with observations, where the QPO data is often fit by a collection of Lorentzian peaks (Nowak 2000; Belloni et al. 2002).

Due to the linear properties of the Fourier transform, the above analysis, while derived assuming a purely sinusoidal signal with a single frequency  $\nu_0$ , can be applied equally well to any periodic light curve with an arbitrary shape. If each coherent section of the light curve is written as

$$f(t) = \sum_j A_j \sin(2\pi\nu_j t + \phi_j), \quad (19)$$

then the total power spectrum (integrating over a distribution of coherent segments with random phase) is simply the sum of the Lorentz-broadened peaks:

$$\begin{aligned} \tilde{I}^2(\nu) &= \int_0^\infty |G(\nu, T)|^2 dN(T) \\ &= 2N_{\text{spot}} A_j^2 \frac{T_l}{T_f} \sum_j \frac{1}{1 + 4\pi^2 T_l^2 (\nu - \nu_j)^2}. \end{aligned} \quad (20)$$

Note that every peak in the power spectrum  $\tilde{I}^2(\nu)$  has the same characteristic width  $\Delta\nu = 1/(2\pi T_l)$ .

The sum in equation (19) can be generalized to a Fourier integral so that (20) becomes the convolution of the segment power spectrum  $F^2(\nu)$  with a normalized Lorentzian  $\mathcal{L}(0, \Delta\nu)$  centered on  $\nu = 0$  with width  $\Delta\nu$ :

$$\tilde{I}^2(\nu) = \int_{-\infty}^{\infty} \frac{F^2(\nu')d\nu'}{1 + \left(\frac{\nu-\nu'}{\Delta\nu}\right)^2} = [F^2 \star \mathcal{L}(0, \Delta\nu)](\nu). \quad (21)$$

Now we can apply our results to the light curves as calculated by the original ray-tracing code for a single geodesic hot spot. First, the X-ray signal over one complete period is calculated to give the Fourier components  $A_j$  in (19). For geodesic orbits, the power spectrum  $F^2(\nu)$  is concentrated at integer combinations of the black hole coordinate frequencies  $\nu_\phi$ ,  $\nu_r$ , and  $\nu_\theta$ . In Schnittman & Bertschinger (2004a) we showed how the Fourier amplitudes depend on orbital inclination and eccentricity as well as hot spot shape and overbrightness. Given these frequencies  $\nu_j$ , amplitudes  $A_j$ , and a characteristic hot spot lifetime  $T_l$ , the integrated power spectrum follows directly from equation (20).

Using the same ray-tracing code, we can also directly simulate the light curve and corresponding power spectrum produced by many hot spots orbiting with random phases, continually formed and destroyed over each time step with probability  $dt/T_l$  (Schnittman & Bertschinger 2004b). The power spectrum of such a simulation is shown in Figure 1 (crosses), along with the analytic model (solid curve). We should stress that this curve is *not a fit to the simulated data*, but an independent result calculated using the model described above. For this particular example, the black hole has mass  $M = 10M_\odot$  and spin  $a/M = 0.5$  with a disk inclination of  $i = 70^\circ$ . Each hot spot is on an orbit with  $\nu_\phi = 285$  Hz,  $\nu_r = 95$  Hz, and a moderate eccentricity of  $e = 0.1$ . This particular orbit was chosen because of the 3:1 ratio in coordinate frequencies, giving the strongest power at the modes  $\nu_\phi - \nu_r : \nu_\phi : \nu_\phi + \nu_r = 2 : 3 : 4$ . Similar frequencies appear to be the dominant peaks in the type A QPOs observed in XTE J1550-564 (Remillard et al. 2002).

The defining characteristic of QPO peaks broadened by the summation of random phases is the uniform width of the individual peaks. For a power spectrum with multiple harmonics and beat modes, each peak is broadened by exactly the same amount, determined by the average lifetime of the individual hot spots. Thus if we can measure the widths of multiple QPO peaks in the data, the hot spot lifetime can be determined redundantly with a high level of confidence.



### 3. DISTRIBUTION OF COORDINATE FREQUENCIES

In the previous section, we assumed a single radius for the hot spot orbits. This assures identical geodesic coordinate frequencies for different hot spots with different phases and lifetimes. However, this assumption betrays one of the major weaknesses of the geodesic hot spot model: there still does not exist a strong physical argument for why these hot spots should form at one special radius or why that radius should have coordinate frequencies with integer commensurabilities. For now, we will be forced to leave that question unanswered, but we can make progress by drawing on intuition gained from other fields of physics. If there does exist some physical resonance in the system that favors these orbits, causing excess matter to “pile up” at certain radii (Abramowicz & Kluzniak 2001, 2003), then just like any other resonance, there should be some finite width in phase space over which the resonant behavior is important. The integer commensurability of the QPO peaks suggests that closed orbits may be playing an important role in the hot spot formation. If this is so, then some hot spots should also form along orbits that *almost* close, i.e. geodesics with nearly commensurate coordinate frequencies. These orbits will have guiding center radii similar to the critical radius  $r_0$  for which the geodesics form closed curves.

Motivated by other processes in nature such as damped harmonic oscillators and atomic transitions, we model the resonance strength as a function of radius with a Lorentzian of characteristic width  $\Delta r$ . Then the probability of a hot spot forming at a given radius is proportional to the strength of the resonance there, giving a distribution of orbits according to

$$P(r)dr = \frac{dr/(\pi\Delta r)}{1 + \left(\frac{r-r_0}{\Delta r}\right)^2}. \quad (22)$$

For a relatively small resonance width  $\Delta r$ , we can linearize the coordinate frequencies  $\nu_j(r)$  around  $r = r_0$  with a simple Taylor expansion:

$$\nu_j(r) \approx \nu_{j0} + (r - r_0) \left. \frac{d\nu_j}{dr} \right|_{r_0}, \quad (23)$$

in which case the probability distribution in frequency space is also a Lorentzian:

$$P(\nu_j)d\nu_j = \frac{d\nu_j/(\pi\Delta\nu_j)}{1 + \left(\frac{\nu_j-\nu_{j0}}{\Delta\nu_j}\right)^2}. \quad (24)$$

Here  $\nu_j = \nu_\phi, \nu_\theta, \nu_r$  are the azimuthal, vertical, and radial coordinate frequencies and  $\nu_{j0} = \nu_j(r_0)$  are those frequencies at the resonance center.

For nearly circular orbits, the coordinate frequencies (using geometrized units with  $G = c = M = 1$ ) are given by Merloni, Vietri, & Stella (1999) [following earlier work by

Bardeen, Press, & Teukolsky (1972); Perez et al. (1997)]:

$$\nu_\phi = \frac{\pm 1}{2\pi(r^{3/2} \pm a)}, \quad (25a)$$

$$\nu_\theta = \nu_\phi \left[ 1 \mp \frac{4a}{r^{3/2}} + \frac{3a^2}{r^2} \right]^{1/2}, \quad (25b)$$

and

$$\nu_r = \nu_\phi \left[ 1 - \frac{6}{r} \pm \frac{8a}{r^{3/2}} - \frac{3a^2}{r^2} \right]^{1/2}, \quad (25c)$$

where the upper sign is taken for prograde orbits and the lower sign is taken for retrograde orbits (the results below assume prograde orbits, but the analysis for retrograde orbits is essentially the same). These frequencies are plotted in Figure 2 as a function of  $r$  for a representative black hole with mass  $10M_\odot$  and spin  $a/M = 0.5$ . The radial frequency approaches zero at the ISCO, where geodesics can orbit the black hole many times with steadily decreasing  $r$ . In the limit of zero spin and large  $r$ , the coordinate frequencies reduce to the degenerate Keplerian case with  $\nu_\phi = \nu_\theta = \nu_r = 1/(2\pi r^{3/2})$ .

Generally, the power spectrum of the periodic light curve from a single hot spot orbiting at  $r_0$  will be made up of delta functions located at the harmonics of the fundamental  $\nu_\phi$  and the beat modes with  $\nu_r$  and  $\nu_\theta$ . Considering for the moment only planar orbits, the power will be concentrated at the frequencies  $\nu = n\nu_\phi \pm \nu_r$ , where  $n$  is some positive integer. In fact, there will be additional peaks at  $\nu = n\nu_\phi \pm 2\nu_r$  and even higher beat-harmonic combinations, but for coordinate frequencies with  $\nu_\phi = 3\nu_r$ , these higher modes are degenerate, e. g.  $\nu_\phi + 2\nu_r = 2\nu_\phi - \nu_r$ . A careful treatment can distinguish between these degenerate modes, but in practice we find the power in the radial double- and triple-beats to be insignificant compared to the single-beat modes at  $n\nu_\phi \pm \nu_r$ , so we limit our analysis to these frequencies.

From equations (23) and (24), we see that a QPO peak centered around  $\nu = n\nu_\phi \pm \nu_r$  will be a Lorentzian of width

$$\Delta\nu = \Delta r \left( n \frac{d\nu_\phi}{dr} \pm \frac{d\nu_r}{dr} \right)_{r_0}. \quad (26)$$

Unlike in the previous section where the random phases gave a single width for every QPO peak, now each peak in the power spectrum will be broadened by a different but predictable amount. Note in particular how the peaks at the higher harmonics with  $n > 1$  will be significantly broader (and thus lower in amplitude) than the fundamental. Another important feature evident from Figure 2 and equation (26) is that, due to the opposite-signed slopes of  $\nu_r(r)$  and  $\nu_\phi(r)$  around  $r_0$ , the beat mode at  $\nu_\phi + \nu_r$  remains very narrow, while the peak at

$\nu_\phi - \nu_r$  is quite broad. These features should play a key role in using the power spectrum as an observable in understanding the behavior of geodesic hot spots.

As in Section 2, the first step in producing a simulated power spectrum is to calculate the Fourier amplitude in each mode with the full three-dimensional ray-tracing calculation of emission from a single periodic hot spot at  $r_0$ . Again, the linear properties of the problem allow us simply to sum a series of Lorentzians, each with a different amplitude, width, and location (peak frequency), to get the total power spectrum. The amplitudes  $A_j$  are given by the ray-tracing calculations, the locations  $\nu_j$  from the geodesic coordinate frequencies and their harmonics, and the widths  $\Delta\nu_j$  from equation (26).

Since the QPO peak broadening is most likely caused by a combination of factors including the hot spots' finite lifetimes as well as their finite radial distribution, the simulated power spectrum should incorporate both features in a single model. Now the computational convenience of Lorentzian peak profiles is clearly evident, since the net broadening is given by the convolution of both effects and the convolution of two Lorentzians is a Lorentzian:

$$[\mathcal{L}(\nu_1, \Delta\nu_1) \star \mathcal{L}(\nu_2, \Delta\nu_2)](\nu) = \mathcal{L}(\nu_{\text{tot}}, \Delta\nu_{\text{tot}})(\nu), \quad (27)$$

where the peak centers and widths simply add:  $\nu_{\text{tot}} = \nu_1 + \nu_2$  and  $\Delta\nu_{\text{tot}} = \Delta\nu_1 + \Delta\nu_2$ . In the case where one or both of the Lorentzians is *not* normalized, the amplitude of the convolved function is given as a function of the individual peak amplitudes and widths:

$$A_{\text{tot}} = \pi \frac{A_1 A_2 \Delta\nu_1 \Delta\nu_2}{\Delta\nu_1 + \Delta\nu_2}, \quad (28)$$

where  $A_1$  and  $A_2$  are the peak amplitudes of the respective Lorentzians [ $A_j = 1/(\pi\Delta\nu_j)$  corresponds to a normalized function.]

Figure 3 shows the simulated power spectrum for a collection of hot spots orbiting near the commensurate radius  $r_0 = 4.89M$  with a distribution width of  $\Delta r = 0.05M$ . All other black hole and orbital parameters are identical to those in Figure 1. Both the random phase broadening described in Section 2 and the effects of a finite resonance width are included in the model. Again, we should stress that the solid line is not a fit to the data, but rather an analytic model constructed from the sum of Lorentzian profiles as described above. In this example, the hot spots have a typical lifetime of 30 orbits, so the random phase broadening contributes only  $\Delta\nu \sim 1.5$  Hz for each peak. This allows us to focus on the effect that a finite resonance width has on the behavior of the QPO peaks at the coordinate frequencies and their various beat harmonics. For a resonance width of  $\Delta r = 0.05M$ , the peak widths due only to coordinate frequency broadening are shown in Table 1.

The narrow peak at  $\nu_\phi + \nu_r = 380$  Hz and the neighboring broad peak at  $2\nu_\phi - \nu_r = 475$  Hz are clearly visible in the simulated data of Figure 3. Precise measurements of each

peak’s width may not come until a next generation X-ray timing mission, but the qualitative behavior shown here should be detectable with the current observational capabilities of RXTE. Combining equations (11) and (26) gives a system of equations that solve for the hot spot lifetime  $T_l$  and the resonance width  $\Delta r$  as a function of the QPO peak widths  $\Delta\nu_j$ . If we could accurately measure the widths of only two peaks, both  $T_l$  and  $\Delta r$  could be determined with reasonable significance. More peaks would give tighter constraints and thus serve to either support or challenge the assumptions of the hot spot model.

#### 4. PHOTON STATISTICS AND CORONAL SCATTERING

Another feature that is important in modeling QPO power spectra is based on the limitations of photon counting statistics by the RXTE instruments. We can easily model this effect using the same ray-tracing program employed above, now selecting only a small random fraction of the rays to make up the light curve at each time step. The resulting light curve is the “standard” light curve, effectively multiplied by a random function in time with amplitude described by a Poisson distribution, analogous to the sampling functions used in Section 2. The corresponding Fourier transform is the collection of original delta functions at the coordinate frequencies, convolved with the transform of a Poisson-valued sampling function.

For a Poisson distributed function  $w(t)$  sampled over  $N$  intervals of  $\Delta t$  with an average value of  $\mu$ , the corresponding Fourier transform  $W(\nu)$  is given by

$$W(\nu) = \begin{cases} \mu & \nu = 0 \\ P(W) & \nu \neq 0 \end{cases}, \quad (29)$$

where for non-zero values of  $\nu$ ,  $W(\nu)$  is a complex random variable with uniformly distributed phase and with amplitude given by the Rayleigh distribution [e. g., Groth (1975)]

$$P(W)dW = \frac{2N}{\mu} W e^{-W^2 N/\mu} dW. \quad (30)$$

The corresponding power  $W^2(\nu \neq 0)$  appears as a background white noise with mean

$$\langle W^2 \rangle = \frac{\mu}{N} \quad (31)$$

and variance

$$\sigma^2[W^2] = 4 \frac{\mu^2}{N^2} \quad (32)$$

constant over all frequencies. Unlike some of the other instrumental contributions to the background power, the Poisson noise is uncorrelated at different frequencies.

As mentioned in the previous sections, the transform of a perfectly periodic time series  $f(t)$  will be zero everywhere except for a finite set of frequencies  $\nu_j$  where  $F(\nu_j) = A_j$ . To compute the simulated power spectrum of  $f(t)$ , multiplied by a Poisson sampling function  $w(t)$ , we must first convolve the transform functions  $F(\nu)$  and  $W(\nu)$  in frequency space and then take the squared amplitude, giving the net power spectrum  $G^2(\nu)$ , which will be composed of the same delta functions that define  $F^2(\nu)$ , scaled by a factor of  $\mu^2$ . In addition to these peaks, there will be a flat background noise function  $G^2(\nu \neq \nu_j)$  with the same type of probability distribution as  $W^2$ . The net power spectrum is then given by

$$G^2(\nu) = \begin{cases} \mu^2 A_j^2 & \nu = \nu_j \\ P(G^2) & \nu \neq \nu_j \end{cases}, \quad (33)$$

where the noise spectrum  $G^2(\nu \neq \nu_j)$  is again a random variable with distribution function

$$P(G^2)dG^2 \propto \exp\left(-\frac{NG^2}{\mu \sum A_j^2}\right) \quad (34)$$

and average power

$$\langle G^2 \rangle = \frac{\mu}{N} \sum_j A_j^2. \quad (35)$$

One significant conclusion from this analysis is that the Poisson sampling noise will not contribute to the broadening of the QPO peaks. Since the Poisson noise is uncorrelated, a random sampling window function combined with *any* light curve [not just the strictly periodic  $f(t)$  used here] will maintain the Fourier properties of the original function  $F(\nu)$  while adding a constant level of background noise characterized by  $P(W)$ . Thus we can confidently apply our analysis from Sections 2 and 3 without worrying about additional broadening from random emission and detection processes. Furthermore, these results give us insights into an equally important part of the QPO power spectrum: the background noise, which is critical when attempting to fit Lorentz functions to the data and determining the amplitude of each significant peak.

From equations (33) and (35), we see that signal  $G^2(\nu = \nu_j)$  to noise  $G^2(\nu \neq \nu_j)$  scales as  $\mu$ , thus giving a stronger detection for higher sampling rates, just as expected. In the context of the hot spot model, we interpret  $\mu$  to be the average fraction of simulated light rays traced from the disk to the detector, so typically  $\mu \ll 1$ . The actual value for  $\mu$  will depend on the spatial and time resolution of the ray-tracing calculation as well as the luminosity and distance to the source in question. For a source like XTE J1550-564 radiating with an intensity of 1 Crab unit, the RXTE photon count rate in the range 2-60 keV is  $\sim 13,000$  counts  $s^{-1}$  (Swank 1998). With a typical QPO amplitude of 1% rms, this corresponds to roughly  $10^{-2} - 10^0$  photons *from the hot spot alone* per 50  $\mu s$  interval.

If the background noise were due purely to Poisson statistics, sufficient binning in the frequency domain would effectively remove the variance of  $G^2$  and allow us to subtract the mean background, leaving a pure signal  $G^2(\nu_j)$ . However, for the proportional counter array instrument on RXTE, there is an additional noise contribution from the effect of detector “deadtime” that must be considered during the data analysis process (van der Klis 1989; Mitsuda & Dotani 1989). This additional correction is particularly important for high count rates. For these high intensity sources, there are a number of other detector contributions that must also be included. In practice, they are generally combined and modeled as a single noise function introduced in the data analysis pipeline, such as a broken power law in frequency.

Another simplified model we have included is that of scattering photons from the hot spot off of a low-density corona of hot electrons around the black hole and accretion disk. This is known to be an important process for just about every observed state of the black hole system (McClintock & Remillard 2004). Unfortunately, it is also an extremely difficult process to model accurately. Fortunately, for the problem of calculating light curves and power spectra, a detailed description of the scattering processes is probably not necessary. The most important qualitative feature of the coronal scattering is a smearing of the hot spot image: a relativistic emitter surrounded by a cloud of scattering electrons will appear blurred, just like a lighthouse shining its beam through dense fog. The effect is even more pronounced in the black hole case, where the hot spot orbital period is of the same order as the light-crossing time of a small corona, thus spreading out the X-ray signal in time as well as space.

Since the scattered photons are often boosted to higher energies, a coherent phase lag in the light curves from different energy channels could be used to estimate the overall scale length of the corona. Vaughan et al. (1997) have observed this effect in neutron star QPOs and infer a scattering length of  $\lambda \sim 5 - 15M$  for an optical depth of  $\tau \sim 5$  in the source 4U 1608-52. Ford et al. (1999) perform a similar analysis for black holes, including the possibility for an inhomogeneous corona, and derive a much larger upper limit ( $\lambda \sim 10^3M$ ) for the size of the corona. In either case, the qualitative effect will be the same: the damping of higher harmonic features in the power spectrum of the X-ray light curve.

The simple model we introduce is based on adding a random time delay to each photon detected from the hot spot. The distribution of this time delay is computed as follows: we fix the optical depth to be unity for scattering through a medium of constant electron density, so each photon is assumed to scatter exactly once between the emitter and the observer, thus determining the length scale of the corona as a function of density. In this case, the

probability of scattering after a distance  $l$  is

$$P(l)dl = \frac{dl}{\lambda} e^{-l/\lambda}, \quad (36)$$

where  $\lambda$  is the photon mean free path in the corona.

Next, due to the likely existence of an optically thick disk around the black hole equator, we assume that the photon scattering angle is less than  $\pi/2$  (we define the scattering angle  $\theta'$  as the angle between the incoming and outgoing wave vectors, so a straight path would correspond to  $\theta' = 0$ ). In other words, only photons emitted in a hemisphere facing the observer can ultimately be scattered in the observer's direction. For a photon emitted at an angle  $\theta$  to the observer, scattering at a distance  $l$  from the source produces an additional photon path length of  $d = l(1 - \cos\theta)$ , assuming for simplicity a flat spacetime geometry. While the photons are emitted with an isotropic distribution in, the scattering distribution is *not* isotropic. Since the scattering geometry requires that  $\theta = \theta'$ , we only detect a subset of the photons emitted with an angular distribution in  $\theta$  that satisfies this relationship. In the limit of low-energy photons ( $h\nu \ll m_e c^2$ ) and elastic scattering, the classical Thomson cross section  $\sigma_T$  is used:

$$\frac{d\sigma}{d\theta'} = \frac{3}{8} \sigma_T \sin\theta' (1 + \cos^2\theta'). \quad (37)$$

Integrating this distribution over all forward-scattered photons ( $\theta' < \pi/2$ ), we find the average additional path length to be  $\langle d \rangle = 7l/16$ . Since the time delay is the path length divided by the speed of light  $c$ , scattering once in the corona adds a time delay  $\Delta t$  to each photon with probability

$$P(\Delta t)d(\Delta t) = \frac{d(\Delta t)}{T_{\text{scat}}} e^{-\Delta t/T_{\text{scat}}}, \quad (38)$$

where the average scattering time is given by  $T_{\text{scat}} = 7\lambda/16c$ .

Applied to the ray-tracing model, this has the effect of smoothing out the light curve with a simple convolution in the time domain of the original signal  $f(t)$  and the time delay probability distribution function  $P(\Delta t)$ . The Fourier transform of the resulting light curve is the product of the two transforms  $F(\nu)$  and  $\tilde{P}(\nu)$ , where

$$\tilde{P}(\nu) = \frac{1}{1 + 2\pi i T_{\text{scat}} \nu}. \quad (39)$$

When we square the product to get the power spectrum  $G^2(\nu) = F^2(\nu)\tilde{P}^2(\nu)$ , the scaling factor is yet again a Lorentzian:

$$G^2(\nu_j) = \frac{A_j^2}{1 + (\nu_j/\Delta\nu_{\text{scat}})^2}, \quad (40)$$

where the scale of frequency damping is given by

$$\Delta\nu_{\text{scat}} \equiv 1/(2\pi T_{\text{scat}}) \quad (41)$$

and  $A_j$  are the delta function amplitudes of  $F(\nu)$  as defined above. This analytic result is perhaps a case where the ends justify the means. Our model for electron scattering in the corona is extraordinarily simplified, ignoring the important factors of photon energy, non-isotropic emission, multiple scattering events in a non-homogeneous medium, and all relativistic effects. However, assuming that almost any analytic model would be equally (in)accurate, at least the treatment we have applied proves to be computationally very convenient.

Equation (40) states that the resulting power spectrum of the scattered light curve is a set of delta functions, with the higher harmonics damped out by the effective blurring of the hot spot beam propagating through the coronal electrons. A simulated power spectrum is shown in Figure 4a for a scattering length of  $\lambda = 10M$ , comparable to the size of the hot spot orbit. Figure 4b shows the effect of a larger, low-density corona with scale length  $\lambda = 100M$ , corresponding to a longer convolution time and thus stronger harmonic damping. The white background noise (Poisson noise with  $\mu = 1$ ) in both cases is due to the statistics of the random scattering of each photon from one time bin to another. The simulated spectra are plotted as dots (asterices at  $\nu_j$  to highlight the peaks) and the analytic model is a solid line.

As in the model for Poisson sampling, we see that the coronal scattering should not contribute to the broadening of the QPO peaks. However, it will have a very significant effect on the overall harmonic structure of the power spectrum, particularly at higher frequencies. Schnittman & Bertschinger (2004a) show a similar result caused by the stretching of the geodesic blob into an arc along its path, also damping out the power at higher harmonics. In this context, it is now clear that the arc damping can be modeled analytically by interpreting the stretching of the blob in space as a convolution of the light curve in time. If the stretched hot spot has a Gaussian distribution in azimuth with length  $\Delta\phi$ , the original X-ray light curve will be convolved with a Gaussian window of characteristic time  $\Delta t = \Delta\phi/(2\pi\nu_\phi)$ . Equation (13) gives the corresponding scaling factor  $W(\nu)$  in the frequency domain (replacing  $T$  with  $\Delta t/2$ ). The exponential damping of  $W(\nu)$  is stronger than the Lorentzian factor at higher frequencies, but both effects (coronal scattering and hot spot stretching) are probably important in explaining the lack of significant power in the harmonics above  $\sim 500$  Hz in the RXTE observations.



## 5. FITTING QPO DATA FROM XTE J1550-564

In this section we combine all the pieces of the model developed above and apply the results to the RXTE data from type A and type B QPOs observed in the low-mass X-ray binary XTE J1550-564. To compare directly with the data from Remillard et al. (2002), we need to change slightly our normalization of the power spectrum. Following Leahy (1983) and van der Klis (1997), we define the power spectrum  $Q(\nu)$  so that the total power integrated over frequency gives the mean square of the discrete light curve  $I_j = I(t_j)$ :

$$\int_{\nu>0}^{\nu_N} Q(\nu) d\nu = \frac{1}{N_s} \sum_{j=0}^{N_s-1} \left( \frac{I_j - \langle I \rangle}{\langle I \rangle} \right)^2, \quad (42)$$

where  $I_j$  is sampled over  $j = 0, \dots, N_s - 1$  with average value  $\langle I \rangle$ . In terms of the power spectra used in Sections 2 and 3,  $Q(\nu)$  is given by

$$\begin{aligned} Q(0) &= 2 \\ Q(\nu) &= 2T_f \frac{\tilde{I}^2(\nu)}{\tilde{I}^2(0)}, \end{aligned} \quad (43)$$

which has units of  $[(\text{rms}/\text{mean})^2 \text{Hz}^{-1}]$ .

As we described in the introduction, the hot spot model is constructed in a number of steps. These steps result in a first approximation for the black hole and hot spot model parameters, after which a  $\chi^2$  minimization is performed to give the best values for each data set.

- The black hole mass and the inclination of the disk are given by optical radial velocity measurements (Orosz et al. 2002). We take  $M = 10.5M_\odot$  and  $i = 72^\circ$  as fixed in this analysis.
- The black hole spin is determined by matching the frequencies of the HFQPOs to the geodesic coordinate frequencies such that  $\nu_\phi = 3\nu_r$  at the hot spot orbit, giving  $a/M \approx 0.5$  for  $\nu_\phi \approx 276$  Hz. The small uncertainties in the measured value of  $\nu_\phi$  can thus be interpreted indirectly as constraints on the mass-spin relationship.
- The orbital eccentricity and hot spot size and overbrightness are chosen to match the total amplitude of the observed fluctuations. We use a moderate eccentricity of  $e = 0.1$ , but find the peak amplitudes are not very sensitive to this parameter (Schnittman & Bertschinger 2004b). The question of overbrightness is still an area of much research, since the nature of the background disk is not well known during the “steep power law”

state that produces the HFQPOS (McClintock & Remillard 2004). In practice, we set the hot spot emissivity constant and then fit an additional steady-state background flux  $I_B$  to the variable light curve.

- The hot spot arc length and the coronal scattering time scale are chosen to fit the relative amplitudes of the different QPO peaks.
- The hot spot lifetime and the width of the resonance around  $r_0$  are chosen to fit the width of the QPO peaks.
- The observed flux gives the detector count rate, which is added to the white noise from the coronal scattering statistics. In practice, for power spectra with sufficient binning statistics (corresponding to long observations in time), the Poisson noise reduces to a flat spectrum which is subtracted from the data before fitting the model parameters.
- As a final step, we include an additional power law component  $\propto \nu^{-1}$  to account for the contribution due to turbulence in the disk [e. g. Mandelbrot (1999)] not accounted for by the hot spot model. Instrumental effects such as the detector deadtime are combined with the turbulent noise to give a simple two-component background spectrum:

$$Q_{\text{noise}}(\nu) = Q_{\text{PL}}\nu^{-1} + Q_{\text{flat}}. \quad (44)$$

After determining the fixed amplitudes  $A_j$  with the ray-tracing calculation, we minimize the  $\chi^2$  fit over the following parameters: orbital frequency  $\nu_\phi$ , hot spot lifetime  $T_l$ , resonance width  $\Delta r$ , scattering length  $\lambda$ , hot spot arc length  $\Delta\phi$ , steady state flux  $I_B$ , and the background noise components  $Q_{\text{PL}}$  and  $Q_{\text{flat}}$ . The best fit parameters are shown in Table 2, along with  $1\sigma$  (68%) confidence limits. These confidence limits are determined by setting  $\Delta\chi^2 < 7.04$ , corresponding to six “interesting” parameters of the hot spot model, holding the noise components constant (Avni 1976; Press et al. 1997). We find that  $Q_{\text{PL}}$  and  $Q_{\text{flat}}$  are almost identical for both data sets, supporting the presumption that they are indeed a background feature independent of the hot spot model.

In Figure 5 we show the observed power spectra for type A and type B QPOs, as reported in Remillard et al. (2002), along with our best fit models. The type A QPOs are characterized by a strong, relatively narrow peak at  $\nu_\phi \approx 280$  Hz, corresponding to  $\nu_\phi$  in our model, with a minor peak of comparable width at  $\nu_\phi - \nu_r \approx 187$  Hz. Type B QPOs on the other hand, have a strong, broad peak around 180 Hz with a minor peak at 270 Hz. This implies a longer arc, damping out the higher frequency modes, and a shorter average lifetime, broadening the peaks. Both types of QPO suggest a very narrow resonance width  $\Delta r$ , yet the current data does not constrain this parameter very well. Thus we assume the

majority of the peak broadening is caused by the addition of multiple hot spots with random phases and a characteristic lifetime of  $\sim 3$  orbits for the type A QPOs and about half that for type B.

We performed a covariance analysis of the parameter space near the  $\chi^2$  minimum to identify the best-constrained parameters and their relative (in)dependence. This analysis confirms what the confidence limits suggest: the best-constrained parameters are the orbital frequency  $\nu_\phi$ , the hot spot lifetime  $T_l$ , the arc length  $\Delta\phi$ , and the background flux  $I_B$ . For the type A QPOs, we find  $\nu_\phi$  and  $T_l$  to be independent, while the arc length and background flux are strongly correlated, so that  $\Delta\phi/I_B$  is positive and roughly constant within our quoted confidence region. This is because, for shorter arcs with fixed emissivity, increasing the arc length will increase the amplitude of the light curve modulation, requiring a larger background flux to give the same QPO amplitude. For the type B QPOs on the other hand, a longer arc length does not significantly amplify the modulation, since in the limit  $\Delta\phi \rightarrow 360^\circ$ , the light curve would remain constant, and thus the parameters  $\Delta\phi$  and  $I_B$  are relatively independent. For both type A and type B QPOs, we find that the resonance width and the coronal scattering length are independent, yet not very well constrained.

The resulting amplitudes and widths of the major QPO peaks are shown in Table 3, along with  $1\sigma$  confidence limits. These amplitudes are given by the analytic model so that the total rms in the peak centered at  $\nu_j$  is

$$\text{rms}_j = \sqrt{2} \frac{A'_j}{A'_0}, \quad (45)$$

where  $A'_0$  is the mean amplitude of the light curve (including the background  $I_B$ ) and  $A'_j$  are the original Fourier amplitudes  $A_j$  given by the ray-tracing code, appropriately scaled according to equations (33) and (40). This is more instructive than measuring the rms directly from  $Q(\nu)$ , which includes background power and instrumental effects uncorrelated to the actual QPO peaks.

In Schnittman & Bertschinger (2004a), the hot spot light curve was added to a steady-state disk with emissivity that scales as  $r^{-2}$ , which provides an estimate of the size and overbrightness of the hot spots required to produce a given (rms/mean) amplitude in the light curve. Considering that most high frequency QPOs are observed with the greatest significance in the 6-30 keV energy band during the steep power-law spectral state (McClintock & Remillard 2004), it seems rather unlikely that the background flux is coming from a thermal, optically thick disk. Even if the flux is originally produced by such a disk, it clearly undergoes significant scattering in a hot corona to give the high temperature power law observed in the photon energy spectrum.

In the context of the model presented here, we can only calculate the fraction of the

total flux that is coming from the hot spots, determined by fitting to the QPO data, without presuming an actual model for the background emission. For XTE J1550-564, we find that the type A hot spot/arcs contribute 8.5% of the flux in the 6-30 keV band, while the type B arcs must contribute significantly more (38%) to give a comparable amplitude. This is due to the longer arc length described above: in the limit of an azimuthally symmetric ring, even infinite brightness would produce no variability.

## 6. DISCUSSION AND CONCLUSIONS

In the context of a geodesic hot spot model, we have developed a few simple analytic methods to interpret the amplitudes and widths of QPO peaks in accreting black holes. The model combines three-dimensional ray tracing calculations in full general relativity with analytic results of basic convolution theory, which are in turn confirmed by simulating the observed light curves of multiple hot spots. Given the Fourier amplitudes of a single hot spot, we have derived a simple formula for the complete QPO power spectrum made up of Lorentzian peaks of varying amplitudes and widths. This power spectrum can then be fit to observed QPO data and used to constrain parameters of the hot spot model, and possibly measure the black hole mass and spin.

For XTE J1550-564, the locations of the HFQPO peaks are well constrained, in turn constraining the spin parameter  $a/M$  when combined with radial velocity measurements of the black hole mass. Based on the presumption that the 3:2 frequency ratio is indeed caused by closed orbits with coordinate frequencies in a 3:1 ratio, an observed mass of  $M = 10.5 \pm 1.0 M_\odot$  and orbital frequency  $\nu_\phi = 276 \pm 5$  Hz would predict a spin of  $a/M = 0.5 \pm 0.1$  (Orosz et al. 2002; Remillard et al. 2002). If reliable, this coordinate frequency method would give one of the best estimates yet for a black hole spin.

The amplitudes of the QPO peaks can be used to infer the arc length of the sheared hot spot and the relative flux contributions from the hot spot and the background disk/corona. The longer arcs seen in type B QPOs are also consistent with the broader peaks: if the hot spots are continually formed and destroyed along special closed orbits, as the emission region gets stretched into a ring, it is more likely to be dissolved or disrupted, giving a shorter characteristic lifetime  $T_l$  and thus broader peaks.

Unfortunately, the quality of the QPO data is not sufficiently high to confirm or rule out the present hot spot model, leaving a number of questions unanswered. By fitting only two or three peaks, we are not able to tightly constrain all the model parameters, particularly the scattering length scale and the resonance width, both of which are most sensitive to

the higher frequency harmonics. Since the high temperature electrons in the corona tend to transfer energy into the scattered photons, measuring the energy spectra of the different QPO peaks would also prove extremely valuable in understanding the emission and scattering mechanisms. This has been done to some degree with the lower frequency region of the power spectra from black holes and neutron stars (Ford et al. 1999), and may even be observable above  $\sim 100$  Hz with current RXTE capabilities. For this analysis to be most effective, a more accurate model for the electron scattering will certainly be necessary.

Some of the power spectrum features discussed in this paper are unique to the geodesic hot spot model, while others could be applied to more general QPO models. Clearly the harmonic amplitudes  $A_j$  given by the ray-tracing calculation are dependent on the hot spot model, as is the broadening from a finite resonance width, yet both could be generalized and applied to virtually any perturbed disk model. Similarly, the random phase broadening and the damping of higher harmonics due to photon scattering will be important effects for any emission mechanism that produces periodic light curves from black holes. If the next generation X-ray timing mission could produce power spectra comparable to the phenomenal cosmic microwave background (CMB) results of recent years, we believe that many of these issues could be resolved. Energy resolution and polarization would similarly provide extremely valuable information about the source of the QPOs. As with the CMB, each successive peak of the power spectrum would help to pin down another parameter until the model becomes *predictive* instead of descriptive, or is ruled out all together.

In the immediate future, however, there is much more to be done with the RXTE data that already exists. Important additional insight might be gained from new analysis of the X-ray light curves in the time domain, recovering some of the phase information lost when the power spectrum is computed in frequency space. There is also an important message in the relationship between the photon energy spectra and the QPO power spectra as well as the connection between the low frequency and high frequency QPOs. Why should the HFQPOs appear in certain spectral states and not others? The answer to these questions may lie in new models of the accretion disk and specifically the radiation physics relating the thermal and power-law emission, as well as broad fluorescent lines like Fe  $K\alpha$ . The fact that the HFQPOs are seen most clearly in the 6-30 keV energy range suggests that standard models of thin, thermal accretion disks are not adequate for this problem. This emphasizes the essential role of radiation transport, particularly through the corona, in any physical model for black hole QPOs.

We thank Ron Remillard for many helpful discussions and providing the QPO data for XTE J1550-564. This work was supported by NASA grant NAG5-13306.

## REFERENCES

- Abramowicz, M. A., & Kluzniak, W. 2001, *A&A*, 374, L19
- Abramowicz, M. A., & Kluzniak, W. 2003, *Gen. Relativ. Gravitation*, 35, 69
- Avni, Y. 1976, *ApJ*, 210, 642
- Bardeen, J. M., Press, W. H., Teukolsky, S. A. 1972, *ApJ*, 178, 347
- Belloni, T., et al. 2002, *ApJ*, 572, 392
- De Villiers, J.-P., Hawley, J. F., & Krolik, J. H. 2003, *ApJ*, 599, 1238
- Ford, E. C. et al. 1999, *ApJ*, 512, L31
- Groth, E. J. 1975, *ApJS*, 29, 285
- Hawley, J. F., & Krolik, J. H. 2001, *ApJ*, 548, 348
- Homan, J., et al. 2004, submitted to *ApJ*, preprint (astro-ph/0406334)
- Lamb, F. K. 2002, in *X-ray Binaries and Gamma-Ray Bursts*, ed. E. P. J. van den Heuvel (San Francisco: Astronomy Society of the Pacific)
- Leahy, D. A., et al. 1983, *ApJ*, 266, 160
- Lee, W. H., & Ramirez-Ruiz, E. 2002, *ApJ*, 577, 893
- Lee, W. H., Abramowicz, M. A., & Kluzniak, W. 2004, *ApJ*, 603, L96
- Mandelbrot, B. B. (1999), *Multifractals and 1/f Noise: Wild Self-Affinity in Physics* (Springer-Verlag: Heidelberg)
- McClintock, J. E., & Remillard, R. A. 2003, in *Compact X-ray Sources*, ed. W. H. G. Lewin & M. van der Klis (New York: Cambridge Univ. Press), in press
- Merloni, A., Vietri, M., Stella, L., & Bini, D. 1999, *MNRAS*, 304, 155
- Mitsuda, K., & Dotani, T. 1989, *PASJ*, 41, 557
- Nowak, M. A., 2000, *MNRAS*, 318, 361
- Orosz, J. A., et al. 2002, *ApJ*, 568, 845
- Orosz, J. A., et al. 2004, submitted to *ApJ*, preprint (astro-ph/0404343)

- Perez, C. A. et al. 1997, *ApJ*, 476, 589
- Press, W. H., et al. 1997, *Numerical Recipes in C: The Art of Scientific Computing* (Cambridge: Cambridge University Press)
- Remillard, R. A., et al. 2002, *ApJ*, 580, 1030
- Remillard, R. A., et al. 2004, submitted to *ApJ*, preprint (astro-ph/0407025)
- Rezzolla, L., Yoshida, S'i., Maccarone, T. J., & Zanotti, O. 2003, *MNRAS*, 344, L37
- Schnittman, J. D., & Bertschinger, E. 2004a, *ApJ*, 606, 1098
- Schnittman, J. D., & Bertschinger, E. 2004b, in *X-Ray Timing 2003: Rossi and Beyond*, ed. P. Kaaret, F. K. Lamb, & J. H. Swank (Melville, NY: American Institute of Physics)
- Stella, L., & Vietri, M. 1998, *ApJ*, 492, L59
- Stella, L., & Vietri, M. 1999, *Phys. Rev. Lett.*, 82, 17
- Stella, L., Vietri, M., & Morsink, S. M. 1999, *ApJ*, 524, L63
- Strohmayer, T. E. et al. 1996, *ApJ*, 469, L9
- Strohmayer, T. E. 2001, *ApJ*, 552, L49
- Swank, J. 1998, in Proceedings of the Symposium “The Active X-Ray Sky: Results from BeppoSAX and Rossi-XTE,” eds. L. Scarsi, H. Bradt, P. Giommi and F. Fiore, *Nucl. Phys. B Proceeding Supplements*, preprint (astro-ph/9802188)
- van der Klis, M. 1989, in *Timing Neutron Stars*, ed. H. B. Ogelman and E. P. J. van den Heuvel (NATO ASI C262: Kluwer)
- van der Klis, M. 1997, in *Statistical Challenges in Modern Astronomy II*, ed. G. J. Babu and E. D. Feigelson, (Springer-Verlag: Berlin)
- Vaughan, B. A. et al. 1997, *ApJ*, 483, L115
- Wagoner, R. V., Silbergleit, A. S., & Ortega-Rodriguez, M. 2001, *ApJ*, 559, L25
- Wang, D. X. et al. 2003, *MNRAS*, 344, 473

Table 1: Widths of QPO peaks around coordinate frequency modes  $n\nu_\phi \pm \nu_r$ , due to a radial distribution of hot spots with  $\Delta r = 0.05M$ . For relatively narrow resonance regions, the QPO peak widths are linearly proportional to  $\Delta r$ . The basic black hole and hot spot model parameters are the same as in Figures 1 and 3.

Mode	Frequency (Hz)	FWHM (Hz)
$\nu_r$	95	3.6
$\nu_\phi - \nu_r$	190	12.2
$\nu_\phi$	285	8.4
$\nu_\phi + \nu_r$	380	4.8
$2\nu_\phi - \nu_r$	475	20.6
$2\nu_\phi$	570	16.8
$2\nu_\phi + \nu_r$	665	13.2

Table 2: Best-fit parameters of the hot spot model for type A and type B QPOs from XTE J1550-564. ( $1\sigma$ ) confidences are shown in parentheses.

Parameter	Type A	Type B
orbital frequency $\nu_\phi$ (Hz)	280.1(2.4)	270.5(12)
lifetime $T_l$ (ms)	10(2.0)	5(1.5)
(orbits)	2.8(0.55)	1.4(0.4)
resonance width $\Delta r$ ( $M$ )	0.02(0.05)	0.025(0.12)
scattering length $\lambda$ ( $M$ )	5(10)	10(20)
arc length $\Delta\phi$ ( $^\circ$ )	155(30)	285(20)
flux ratio $\frac{I_{\text{hotspot}}}{I_B + I_{\text{hotspot}}}$	0.085(0.025)	0.38(0.05)



Table 3: Amplitudes and widths of type A and type B QPO peaks from XTE J1550-564, as determined by the best fit parameters listed in Table 2 and equation (45). ( $1\sigma$ ) confidences are shown in parentheses.

Mode	A		B	
	rms (%)	FWHM (Hz)	rms (%)	FWHM (Hz)
$\nu_r$	0.57(0.15)	33.1(6.2)	2.03(0.21)	63.6(16.0)
$\nu_\phi - \nu_r$	1.62(0.26)	35.7(5.9)	2.57(0.14)	67.6(15.5)
$\nu_\phi$	3.35(0.17)	34.6(5.5)	1.48(0.24)	65.9(15.3)
$\nu_\phi + \nu_r$	0.75(0.19)	33.4(5.8)	0.06(0.02)	64.1(15.8)

Fig. 1.— Simulated power density spectrum (crosses) from a ray-tracing calculation of many hot spots on geodesic orbits with random phases and different lifetimes, along with an analytic model (solid line) of that power spectrum. The black hole has mass  $M = 10M_{\odot}$  and spin  $a/M = 0.5$ , giving  $\nu_r = 95$  Hz and  $\nu_{\phi} = 285$  Hz. The hot spot orbit has an eccentricity of 0.1 around a radius of  $r_0 = 4.89M$  and an inclination of  $70^{\circ}$ . The peaks have Lorentzian profiles with  $\Delta\nu \approx 11$  Hz, corresponding to a characteristic hot spot lifetime of four orbits.

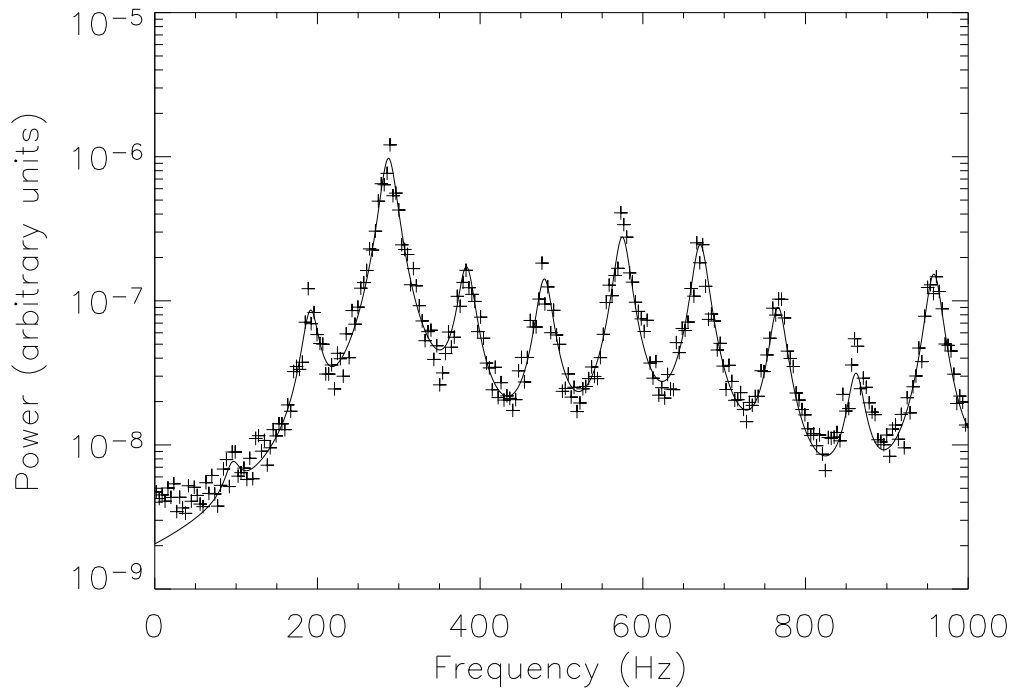


Fig. 2.— Geodesic coordinate frequencies as a function of radius for a black hole with mass  $M = 10M_\odot$  and spin  $a/M = 0.5$ . The radius of the inner-most stable circular orbit  $r_{\text{ISCO}}$  is where  $\nu_r \rightarrow 0$ . The commensurate radius  $r_0$  is where the ratio of azimuthal to radial coordinate frequencies is 3:1.

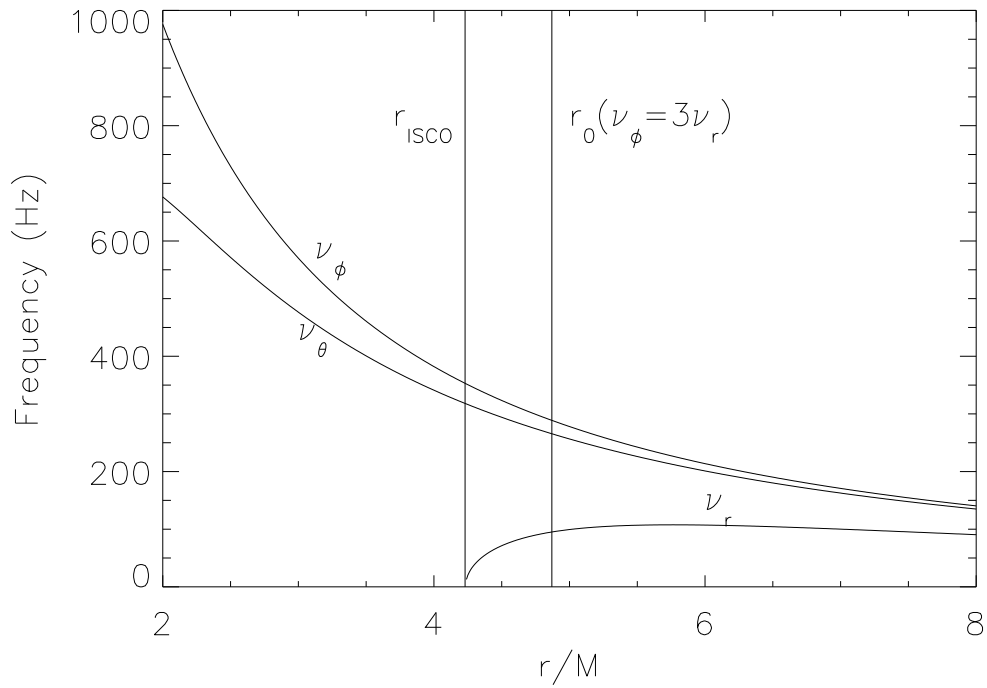


Fig. 3.— Power density spectrum (crosses) from a ray-tracing calculation of many hot spots on geodesic orbits with different radii  $r$  and thus different coordinate frequencies, along with an analytic model (line) of that power spectrum. The black hole has mass  $M = 10M_{\odot}$  and spin  $a/M = 0.5$ , while the average hot spot orbit has an eccentricity of 0.1 around a radius of  $r_0 = 4.89M$ , as in Figure 1. The peaks have Lorentzian profiles with  $\Delta\nu$  given by equations (11) and (26) with  $T_l = 100$  ms and  $\Delta r = 0.05M$ .

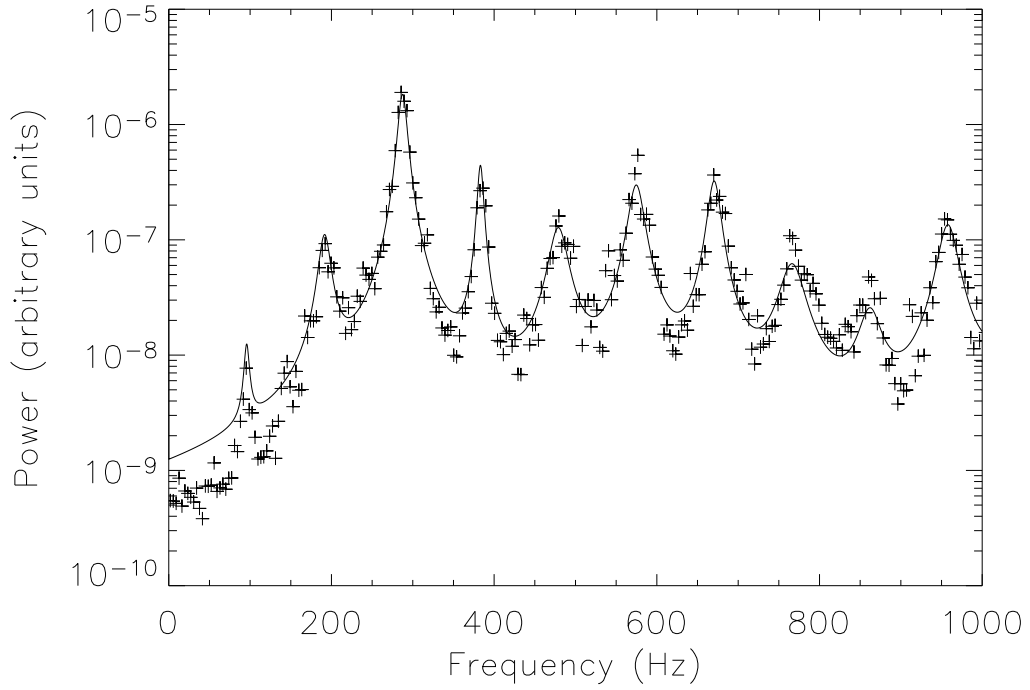


Fig. 4.— Power density spectrum from a single hot spot light curve where the emitted photons are scattered exactly once each by a uniform corona of electrons. The simulated spectra are plotted as dots and asterices, while the analytic model is a solid line. In (a), the mean free path to scattering is  $\lambda = 10M$ , while (b) represents a much larger, low density corona with  $\lambda = 100M$ .

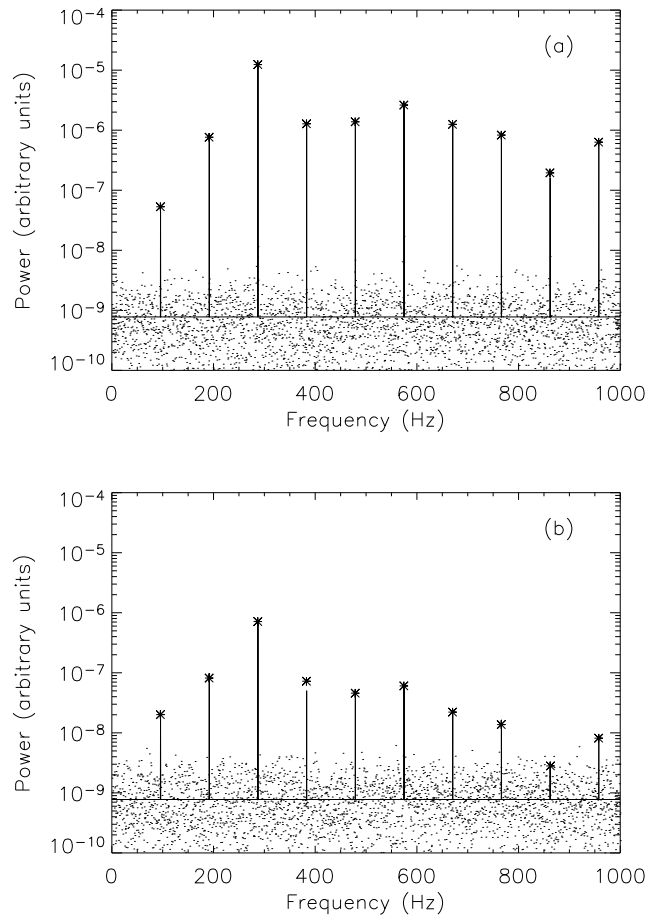


Fig. 5.— Comparison of hot spot model power spectrum (line) with data (crosses) from XTE J1550-564. (a) Type A QPO, dominated by a narrow peak at  $\nu_\phi \approx 280$  Hz. (b) Type B QPO, dominated by a broad peak at  $\nu_\phi - \nu_r \approx 180$  Hz. The best fit model parameters for each data set are shown in Table 2 and the resulting QPO amplitudes and widths are shown in Table 3.

